

Co₂SeO₃Cl₂: Studies of Emerging Magnetoelectric Coupling in a Polar, Buckled Honeycomb Material

Faith O. Adeyemi¹, Xudong Huai¹, Mohamed Kandil², Pradip Karki²,
Wencan Jin², and Thao T. Tran^{1,3*}

¹Department of Chemistry, Clemson University, Clemson, SC 29634, US

²Department of Physics, Auburn University, Auburn, AL 36849, US

³Department of Physics and Astronomy, Clemson, SC 29634, US

*thao@clemson.edu

Abstract:

The development of magnetoelectric materials requires chemical design strategies that integrate structural polarity with magnetic lattices capable of supporting competing spin interactions. Here, we demonstrate such an approach in the polar, buckled honeycomb magnet Co₂SeO₃Cl₂. Magnetization and heat-capacity measurements reveal strong magnetic anisotropy and four successive magnetic transitions at 25.4, 16.8, 11, and 3 K. The recovered magnetic entropy through the ordering regime is only around half of the expected $2R\ln(2)$, indicating persistent spin fluctuations. Second-harmonic generation measurements show three pronounced intensity anomalies at 11, 17, and 26 K that coincide with magnetic transitions while revealing that the crystallographic symmetry is preserved. Together, these results demonstrate that polar, buckled honeycomb magnets offer an unconventional phase space for coupling magnetic and electric dipoles in magnetoelectric materials.

1. Introduction

Frustrated magnets are of significant interest because competing exchange interactions at similar energy scales prevent spins from settling into a conventional magnetic order, potentially resulting in quantum fluctuations and novel states of matter.¹⁻¹⁶ Introducing electric polarity into such frustrated frameworks makes this class of materials even more compelling. A polar magnetic material displays an intrinsic, macroscopic electric dipole while promoting asymmetric magnetic exchange interactions in the presence of isotropic Heisenberg exchange.¹⁷⁻²⁰ Such polar, frustrated systems with appreciable asymmetric coupling can promote antiferromagnetic (AFM) and ferromagnetic (FM) interactions at comparable energies in ways that may be inaccessible in centrosymmetric counterparts. The ability to place magnetic spins in a polar, frustrated lattice opens a new path beyond conventional approaches to magnetoelectric coupling. Such materials can enable electric-field control of magnetic order, magnetic-field tunability of electric polarization, and enhanced sensitivity of both order parameters near phase transitions.^{21, 22} However, achieving such magnetoelectric coupling remains elusive owing to an inherent energy-

scale disparity between magnetic and electric dipoles. Recent studies on two-dimensional magnetoelectric materials, such as NiI₂ for electromagnon physics, light–spin coupling, and prospective opto-spintronic devices,²³⁻²⁵ and NiPS₃ for optical spin readout and magneto-optical modulation, highlight the tunability accessible in reduced dimensions.²⁶⁻²⁸ However, these systems often suffer from modest second-harmonic generation (SHG) signals. Three-dimensional materials, such as Co₄Nb₂O₉, MnWO₄, and BiFeO₃, provide greater SHG responses but typically exhibit less tunability than two-dimensional systems.²⁹⁻³⁴ This trade-off underscores the need for a new chemical design strategy to realize polar, frustrated magnets that promote appreciable magnetoelectric coupling.

One effective strategy is to combine lone-pair-active building group with mixed-ligand coordination. Stereoactive lone-pair asymmetric subunits can induce global polarity if their local electric dipoles add to the overall polarization. At the same time, mixed ligands can generate local polarization at the magnetic site. To examine this design strategy, we create Co₂SeO₃Cl₂—a new polar, frustrated magnet that crystallizes in the monoclinic space group *P2*₁ and features a buckled honeycomb network of Co²⁺ ions. The structure incorporates both O²⁻ and Cl⁻ ligands within the Co coordination environment, while the Se⁴⁺ cation with its stereochemically active lone pair induces pronounced asymmetric distortions that enhance intrinsic polarity. Magnetic susceptibility measurements reveal pronounced magnetic anisotropy and four magnetic transitions. Heat capacity confirms the four transitions. SHG measurements confirm the non-centrosymmetric crystal structure and exhibit five phase transitions, of which three coincide with three magnetic transitions.

2. Results and discussion

2.1. Crystal Structure

Co₂SeO₃Cl₂ crystallizes in a non-centrosymmetric monoclinic lattice (space group *P2*₁). The magnetic Co²⁺ atoms occupy two crystallographically distinct sites, forming buckled honeycomb layers, with the Co-Co distances ranging from 3.5127(6) to 3.9501(5) Å (Figure 1). The buckled honeycomb lattice is formed by alternating Co(1) and Co(2) within the *ac*-plane. Each Co atom is bonded to three O atoms of SeO₃ subunits and three Cl atoms, forming a distorted, polar octahedron [CoO₃Cl₃]. The Co-O bond distances range from 1.953(6) to 2.257(8) Å, and the Co-Cl bond lengths range from 2.450(4) to 2.506(3) Å. Each [Co(1)O₃Cl₃] unit is connected to [Co(2)O₃Cl₃] through edge-sharing along the *c*-axis and corner-sharing along the *a*-axis (Figure 1c). The SeO₃²⁻ trigonal pyramidal group exhibits stereoactive lone-pair electrons with a local electric dipole. The Se atom has the +4 oxidation state with Se–O bond distances 1.711(7) < *d* < 1.720(49) Å. The local polarities of [Co(1)O₃Cl₃], [Co(2)O₃Cl₃], and SeO₃²⁻ units add up, resulting in an overall polar crystal structure along the *b*-axis.

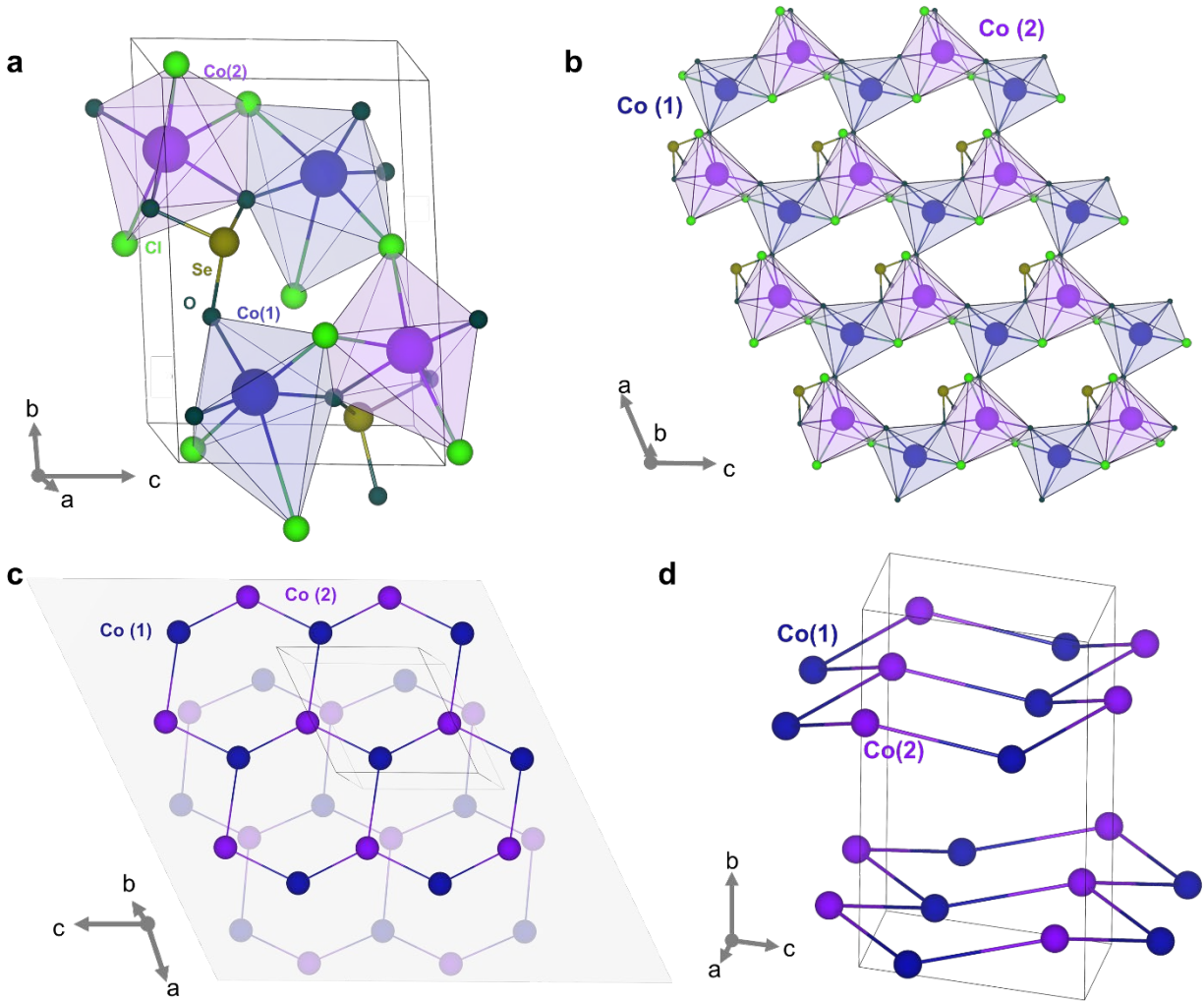


Figure 1 (a) Crystal structure of $\text{Co}_2\text{SeO}_3\text{Cl}_2$; (b) Corner-sharing and edge-sharing network of CoO_3Cl_3 distorted, polar octahedra; (c) Honeycomb magnetic sublattice of the two distinct Co^{2+} ; (d) Sideview showing the buckle honeycomb magnetic sublattice

2.2. Physical Properties

Temperature-dependent magnetization measurements (Figures 2a-b) along different crystallographic directions reveal pronounced magnetic anisotropy and four magnetic transitions at $T_{N1} = 25.4$ K, $T_{N2} = 16.8$ K, $T_{N3} = 11$ K, and $T_{N4} = 3$ K. Upturns in the $\chi(T)$ curves are observed after the onset of AFM ordering, suggesting competing AFM-FM interactions. Upon application of an external magnetic field, the transitions at T_{N1} and T_{N3} shift to higher temperatures, while those at T_{N2} and T_{N4} are suppressed to lower temperatures and eventually disappear by $\mu_0 H = 7$ T. The shift to higher temperatures for the T_{N1} and T_{N3} transitions suggests that the spin entropy of FM coupling is reduced, which is compensated by an increase in the lattice entropy.

To account for the pronounced magnetic anisotropy arising from sizable spin-orbit coupling (SOC) of Co, we analyzed the magnetic susceptibility data using a modified Curie-Weiss (mCW) model.

$$\chi_\alpha(T) = \chi_{0,\alpha} + \frac{C_0}{T-\theta_\alpha} \frac{J_{\text{eff}}(J_{\text{eff}}+1)}{0.75} [w \mu_{1,\alpha}^2(T) + (1-w) \mu_{2,\alpha}^2(T)] \quad (1)$$

$$C_0 = N_A \mu_B^2 / 3k_B \quad (2)$$

$$\mu_{i,\alpha}^2(T) = \frac{\mu_{0,i,\alpha}^2 + \mu_{1,i,\alpha}^2 e^{-\Delta_i/T}}{1 + e^{-\Delta_i/T}} \quad (i = 1, 2) \quad (3)$$

Where $\chi_\alpha(T)$ is the temperature- and orientation-dependent magnetic susceptibility, $\chi_{0,\alpha}$ is the temperature-independent diamagnetic and Van Vleck contribution, θ_α is the modified Weiss constant for axis α , J_{eff} is the effective total spin number, w is the fractional amplitude of Co(1) and Co(2), $\chi_{i,\alpha}(T)$ is the single-ion moment for Co on site i , and $\chi_{0,i,\alpha}$ and $\chi_{1,i,\alpha}$ are the orientation-projected moments of the ground state and the first excited state on site i , and Δ_i is the SOC gap.

The fit in the temperature range of $200 \text{ K} \leq T \leq 300 \text{ K}$ yields characteristic single-ion energy scales of $\Delta_1 = 148 \text{ K}$ ($J_{\text{eff}} = 1/2$ states populated) and $\Delta_2 = 567 \text{ K}$ ($J_{\text{eff}} = 3/2$ states active and $J_{\text{eff}} = 5/2$ unpopulated within the fitting temperature window). The resulting Weiss constants $\theta_a = -62(8) \text{ K}$, $\theta_b = -67(7) \text{ K}$, and $\theta_c = -28(1) \text{ K}$ indicate a net AFM interaction and magnetic anisotropy (Table S1). The effective magnetic moment per Co extracted from the conventional Curie-Weiss analysis of a powder sample is $5.16(7) \mu_B$, which falls between the expected values $4.74 \mu_B$ ($S = 3/2$ and $L = 1$) and $5.67 \mu_B$ ($S = 3/2$ and $L = 2$). The orientation-dependent moments extracted are $5.6(1)$, $5.5(3)$, and $4.4(6) \mu_B$, with $\mu_0 H \parallel a$, b , and c -axis, respectively. The largest value obtained along a likely arises from enhanced orbital contributions, as evidenced by the extracted effective g -factor $g_{\text{eff}} = 2.9$ along a , larger than $g_{\text{eff}} = 2.5$ along b and $g_{\text{eff}} = 2.2$ along c . Overall, the g_{eff} values are significantly higher than the expected spin-only value $g = 2$, confirming appreciable SOC.

$M(H)$ curves at different temperatures reveal linear correlations, indicating AFM dominant interactions. Figure 2d shows ΔS_{mag} derived from the Maxwell relation. The transition at T_{N1} corresponds to a negative entropy change, whereas those at T_{N2} and T_{N3} are associated with positive entropy changes. The transition at T_{N4} first exhibits a negative entropy change at low fields, but then shows a positive entropy change at higher fields.

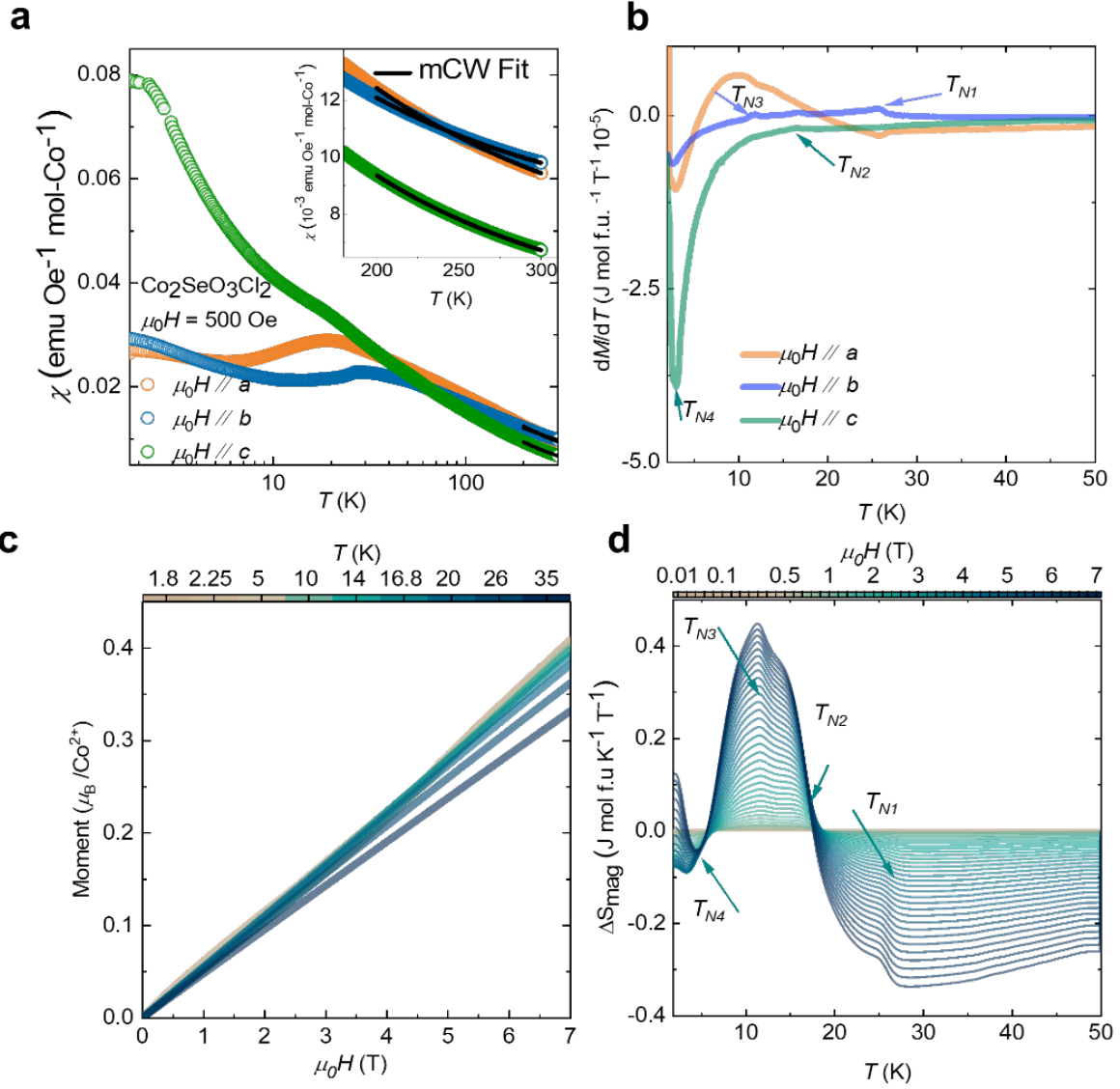


Figure 2. $\text{Co}_2\text{SeO}_3\text{Cl}_2$ (a) Orientation-dependent magnetic susceptibility vs. temperature with modified Curie-Weiss analysis at $\mu_0H = 500$ Oe; (b) Orientation-dependent dM/dT vs. T at $\mu_0H = 500$ Oe; (c) $M(H)$ of powder sample at different temperatures. (d) Magnetic entropy change (ΔS_{mag}) at different magnetic fields at $1.8 \text{ K} \leq T \leq 50 \text{ K}$

To confirm these observed magnetic transitions, heat capacity was measured on $\text{Co}_2\text{SeO}_3\text{Cl}_2$ with $1.8 \text{ K} \leq T \leq 300 \text{ K}$, and $0 \text{ T} \leq \mu_0H \leq 9 \text{ T}$. The heat capacity data confirm the four magnetic transitions observed from the magnetization data. At zero field, the phonon contribution was modeled by fitting the high-temperature heat-capacity data ($45 \text{ K} \leq T \leq 300 \text{ K}$) using a sum of one Debye mode and two Einstein modes as follows:

$$\frac{C_p}{T} = \frac{C_{\text{Debye}(1)}}{T} + \frac{C_{\text{Einstein}(1)}}{T} + \frac{C_{\text{Einstein}(2)}}{T} \quad (5)$$

$$C_{\text{Debye}} = 9NR_S D \left(\frac{T}{\theta_D} \right)^3 D(\theta_D/T) \quad (6)$$

$$C_{Einstein} = 3NRs_E \frac{(\theta_E/T)^2 \exp(\theta_E/T)}{[\exp(\theta_E/T)-1]^2} \quad (7)$$

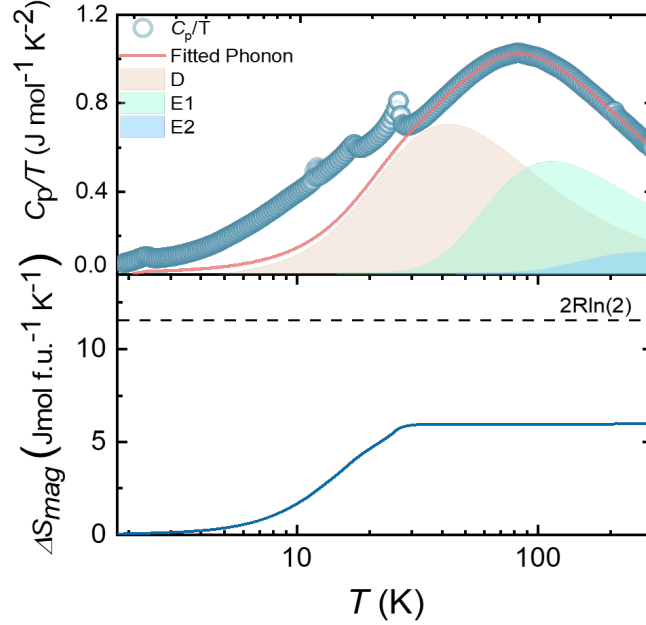


Figure 3. Molar heat capacity over temperature (C_p/T) vs. temperature for $\text{Co}_2\text{SeO}_3\text{Cl}_2$ at $\mu_0H = 0$ T and calculated phonon. The anomalies are consistent with the four magnetic phase transitions. Magnetic entropy change (ΔS_{mag}) compared to the expected value of $J_{\text{eff}} = 1/2$ ($2 * R \ln 2$).

where N represents the number of atoms, R is the gas constant, T is the sample temperature, s_D is the number of oscillators of acoustic phonons, θ_D is the Debye temperature, $D(\theta_D/T)$ is the Debye function, s_E is the number of oscillators of optical phonons. The fitted parameters are summarized in Table S1. The assessment of the phonon is based on the resulting good fit and physical oscillator terms. The fitted total number of oscillators is 7.7(8), close to the total number of 8 atoms per formula unit for $\text{Co}_2\text{SeO}_3\text{Cl}_2$. The presence of an Einstein contribution is justified by the characteristic maximum in C_p/T^3 vs. T (Fig. S3). After subtracting the phonon contribution, the magnetic entropy change was estimated to be 5.9(2) $\text{J mol}^{-1} \text{ f.u.}^{-1} \text{ K}^{-1}$, only 51.2% of the expected value $2 * R \ln 2 = 11.57 \text{ J mol}^{-1} \text{ f.u.}^{-1} \text{ K}^{-1}$ and 25.6% of $2 * R \ln 4 = 23.05 \text{ J mol f.u.}^{-1} \text{ K}^{-1}$. The significant missing entropy observed from the analysis may arise from underestimated phonons or hidden entanglement between spins.

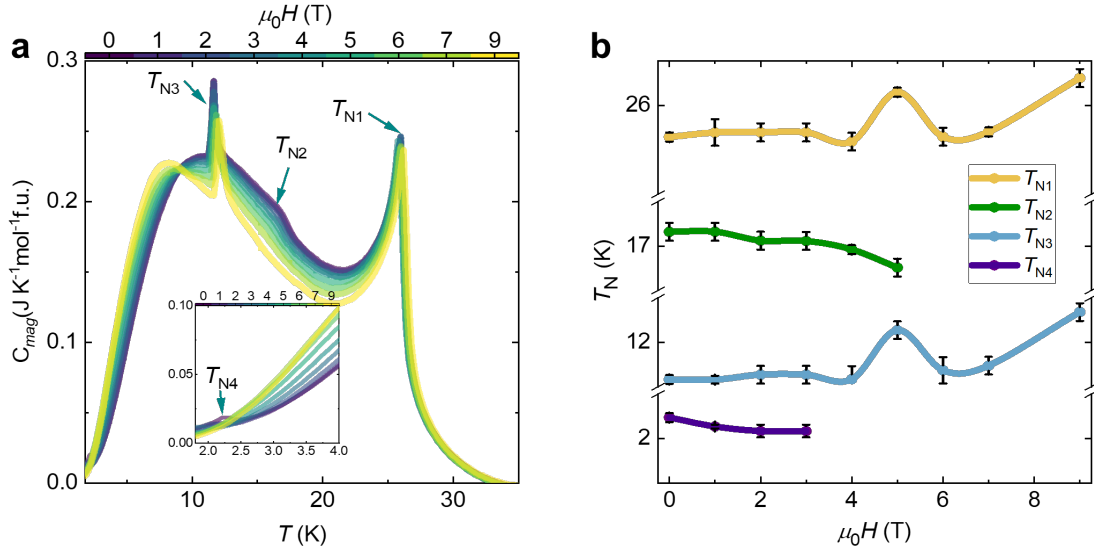


Figure 4. (a) Magnetic contribution to the heat capacity, $C_{\text{mag}}(T)$, measured under applied magnetic fields $\mu_0 H = 0$ –9T. The inset highlights the low-temperature region. (b) Field-dependence of the four transition temperatures.

The magnetic contribution to the heat capacity, C_{mag} , exhibits a pronounced field dependence. Figure 4a shows how C_{mag} evolves under applied fields between 1.8 and 30 K. Overall, transitions at T_{N2} and T_{N4} are progressively suppressed and eventually vanish, while T_{N1} and T_{N3} shift to higher temperatures as magnetic field increases (Figure 4b). This result is consistent with the magnetic susceptibility data.

2.3. Second Harmonic Generation

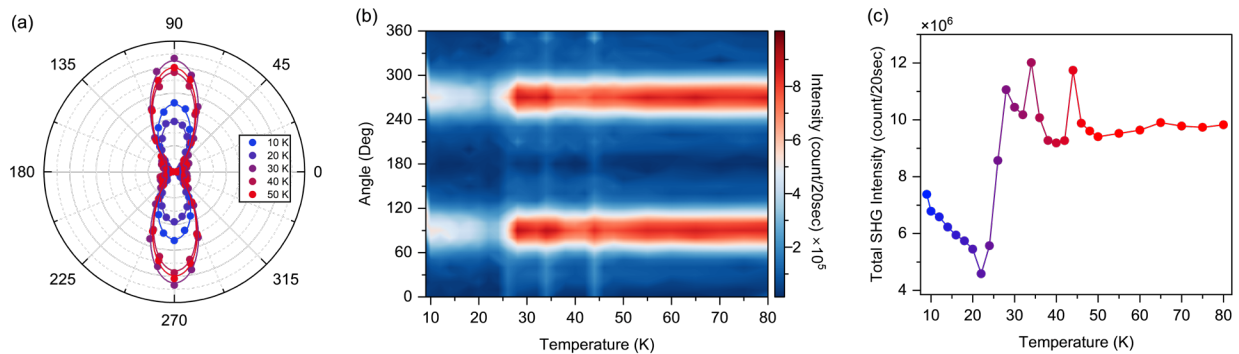


Figure 5 (a) RA-SHG patterns measured in the parallel polarization configuration at selected temperatures across the magnetic transitions; (b) Two-dimensional colormap of the SHG intensity as a function of incident polarization angle and temperature; (c) Temperature dependence of the total SHG intensity obtained by integrating the signal over all polarization angles.

Rotational-anisotropy second-harmonic generation (RA-SHG) patterns were collected between 8 and 300 K, and the results are reproducible across consecutive thermal cycles. As shown in Figure

5a, the patterns can be fitted to a bulk electric dipole radiation in the polar C_2 point group. While the angular dependence of the RA-SHG patterns remains unchanged through the entire temperature range, anomalies in the SHG intensity are observed at multiple temperatures. As shown in Figures 5b-c, the most prominent feature is a sudden jump in SHG intensity at ~ 20 K during warming. In addition, multiple intensity spikes are observed at approximately 26 K, 34 K, and 44 K. These results suggest the presence of multiple phase transitions in the 10–50 K temperature window, which quantitatively modify nonlinear susceptibility tensor elements but do not change crystalline point group symmetry. It is noteworthy that the intensity spikes at 11, 20, and 26 K are in good agreement with the magnetic-driven AFM transitions, suggesting potential coupling between the electronic and magnetic dipoles.

2.4. Computational Studies

Spin-Polarized Band Structure and Density of States

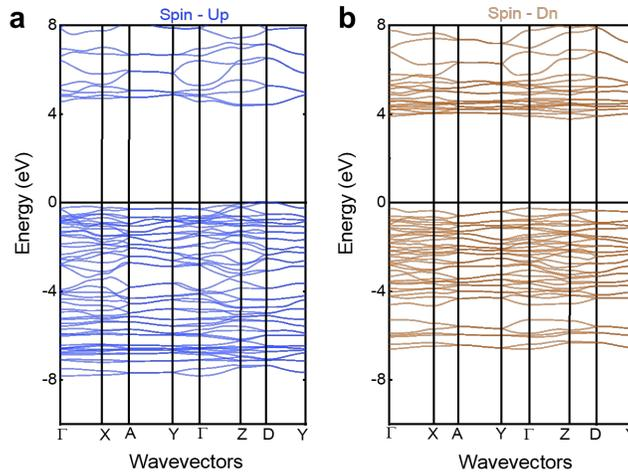


Figure 6. Spin-polarized band structure of $\text{Co}_2\text{SeO}_3\text{Cl}_2$

The electronic structure of $\text{Co}_2\text{SeO}_3\text{Cl}_2$ was investigated using spin-polarized DFT calculations. Strong hybridization between Co-d and O-p/Cl-p interacting atomic wavefunctions produces diffuse bands near the Fermi level (E_F). The density of states (DOS) shows that the majority spin (spin-up) of Co-d is fully occupied, while the minority spin (spin-down) is partially filled at the valence-band edge, consistent with the spin configuration of Co^{2+} ($3d^7$, $S = 3/2$) (Figure 7). The valence band maximum is mostly dominated by Co-d, O-p, and Cl-p states. The O-p states are more dispersed compared to the Cl-p states because of the mixing between the O-p and Se-p states. The presence of Se-p states near E_F indicates Se-s/p mixing of stereoactive lone-pair electrons. The conduction band minimum is mainly derived from the Co-d, O-p, and Se-p states.

The appreciable overlap between Co-d and O-p/Cl-p, along with the contrast in the bandwidths of O-p and Cl-p, may promote sizable competing exchange interactions, magnetic anisotropy, and magnetoelectric coupling.

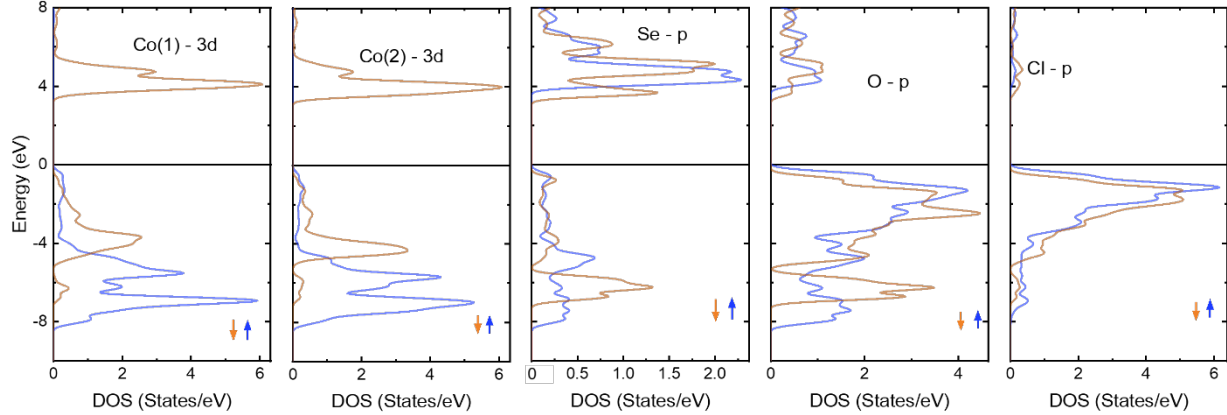


Figure 7. Spin-polarized density of states (DOS) of $\text{Co}_2\text{SeO}_3\text{Cl}_2$

Chemical Bonding

Crystal orbital Hamilton population (COHP) analysis was performed on the relevant atom pairs (Co-O, Co-Cl and Se-O) to understand the relationship between bonding and physical properties in $\text{Co}_2\text{SeO}_3\text{Cl}_2$ (Figure 8).^{37, 38} Co-O, Co-Cl, and Se-O bonds exhibit antibonding contributions ($-\text{pCOHP} < 0$) near the E_F . The electronic instability may prompt the system to evolve into new states of matter under external perturbations. To further quantify the bonding strength, integrated COHP (ICOHP) values were evaluated. Co-O bonds exhibit a larger (more negative) ICOHP value than the Co-Cl bonds, implying stronger hybridization. Se-O bonds display the largest (most negative) ICOHP value, indicating the most covalent bonding character compared to Co-O and Co-Cl bonds. Complementary COBI analysis reveals that Co-Cl and Se-O bonds exhibit almost a single bond (~ 0.9) and slightly more one-and-a-half bond (~ 1.6), respectively. These bond orders are higher than that of Co-O (~ 0.15). The ICOBI results reveal stronger covalent bonding character for Co-Cl and Se-O, and stronger ionic bonding character for Co-O. Overall, the ability to modify bonding characters within the polar, buckled honeycomb magnet using mixed ligands offers a chemical tool to promote cross-coupling between magnetic and electric components.

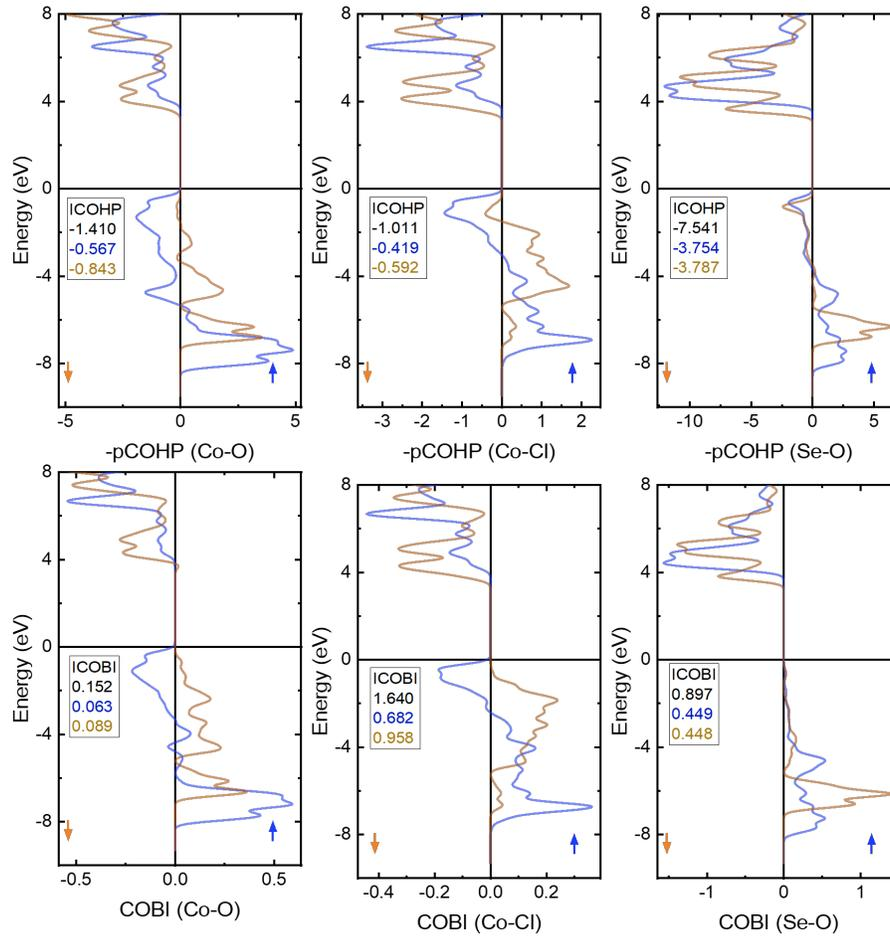


Figure 8. Crystal orbital Hamilton population (COHP) and integration (ICOHP), and crystal orbital bond index (COBI) for Co-O, Co-Cl, Se-O bonds in $\text{Co}_2\text{SeO}_3\text{Cl}_2$.

Spin Density Map

The spin density map projected onto the (010) plane shows that the spin is strongly polarized on Co-3d and then polarizes O-p/Cl-p (Figure 9). The projection onto the (010) plane that cuts through a honeycomb layer reveals strong spin polarization, demonstrating the dominance of intralayered Co–O–Co and Co–Cl–Co superexchange pathways. On the other hand, the projection onto the (010) plane that goes between the honeycomb layers shows weaker but non-zero spin polarization, suggesting finite interlayered superexchange interactions.

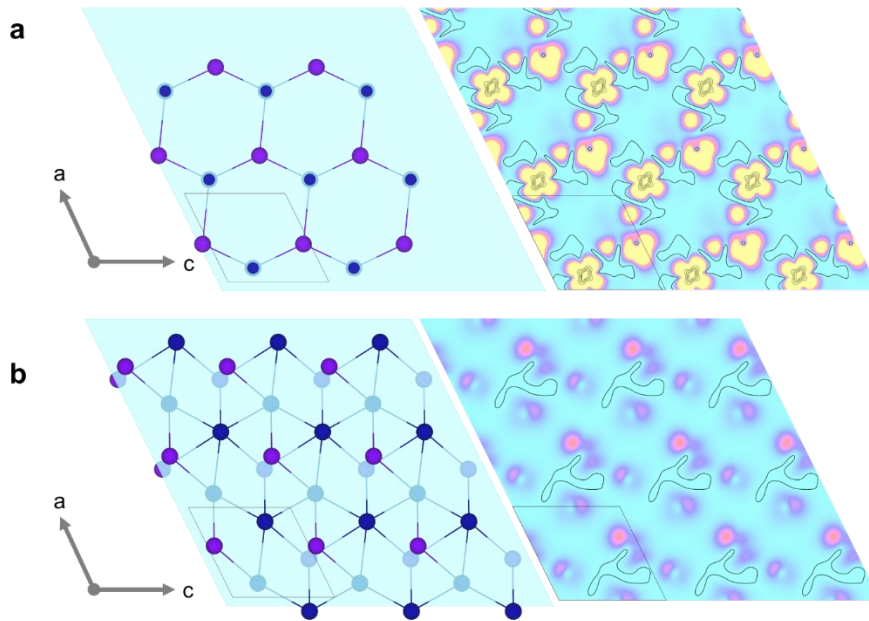


Figure 9. Spin density map of $\text{Co}_2\text{SeO}_3\text{Cl}_2$ (a) Projection onto the (010) plane cutting through the intralayer of Co; (b) Projection onto the (010) plane cutting through the interlayer of Co.

Magnetic Exchange Interactions

The calculated magnetic exchange interactions provide insight into intralayer and interlayer interactions (Figure 10). Within the honeycomb layer where Co-Co separations $\sim 3.4\text{-}3.9 \text{ \AA}$, intralayer magnetism is dominated by antiferromagnetic interactions with $J_1 = -49$, $J_2 = -45$, and $J_4 = -23 \text{ K}$, respectively. Interlayer exchange interactions are generally weaker AFM interactions with $J_3 = -27$, $J_5 = -6$, and $J_6 = -5 \text{ K}$, respectively. The resulting J values are consistent with the observed exchange pathways in the spin-density map. We acknowledge that this calculation, based solely on the Heisenberg model, would not be the most accurate way to describe exchange interactions in the polar, frustrated magnet, where Dzyaloshinskii–Moriya and other anisotropic interactions may be important. The results are intended to provide some hints pointing to overall dominant AFM interactions, which are consistent with the magnetic properties.

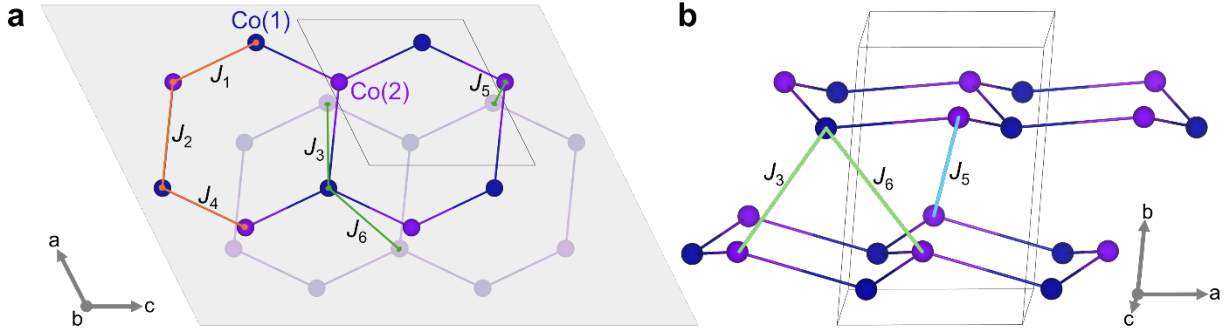


Figure 10. (a) Intralayer and (b) interlayer magnetic exchange interactions

3. Conclusion

Our results demonstrate that the polar, magnetic, buckled honeycomb material $\text{Co}_2\text{SeO}_3\text{Cl}_2$ offers an unconventional space for cross-coupling between magnetic and electric quantities. In contrast to the traditional planar honeycomb system, this material exhibits three common transitions, as observed in magnetic susceptibility and SHG measurements. These transitions are also confirmed by heat capacity data. In addition, $\text{Co}_2\text{SeO}_3\text{Cl}_2$ features mixed J -states and strong quantum fluctuations. Chemical bonding analysis shows the ability to modify bonding characters, bonding anisotropy, and magnetic and electric coupling pathways within this system. Additional characterizations are required to understand the microscopic origins of the potential emerging magnetoelectric coupling. This work establishes a new pathway to overcome the energy-scale mismatch and stabilize magnetoelectric interactions in ways that may be inaccessible in conventional systems.

Acknowledgement.

The work at Clemson University was supported by the NSF CAREER award NSF-DMR-2338014. X.H. and T.T.T acknowledge support from the Arnold and Mabel Beckman Foundation and the Camille Henry Dreyfus Foundation. W. J. acknowledges support by the Air Force Office of Scientific Research under Award No. FA9550-231-0499 and the NSF CAREER Award under Grant No. DMR-2339615.

References

(1) Pressley, L. A.; Sarkis, C. L.; Felder, J.; Dela Cruz, C. R.; Unocic, R. R.; Gai, Z.; Einkauf, J. D.; Pethe, S. P.; Paranthaman, M. P.; Berlijn, T.; et al. Synthesis and Characterization of Metastable

- Cobalt Honeycomb KCoAsO_4 . *Inorg Chem* **2025**, *64* (27), 13696-13704. DOI: 10.1021/acs.inorgchem.5c00932 From NLM PubMed-not-MEDLINE.
- (2) Ito, M.; Haraguchi, Y.; Motohashi, T.; Saito, M.; Ogawa, S.; Ikuta, T.; Katori, H. A. Crystalline water intercalation into the Kitaev honeycomb cobaltate $\text{Na}_2\text{Co}_2\text{TeO}_6$. *Physical Review Materials* **2025**, *9* (9). DOI: 10.1103/nyd3-dt8j.
- (3) Mukharjee, P. K.; Shen, B.; Erdmann, S.; Jesche, A.; Kaiser, J.; Baral, P. R.; Zaharko, O.; Gegenwart, P.; Tsirlin, A. A. Intermediate field-induced phase of the honeycomb magnet $\text{BaCo}_2(\text{AsO}_4)_2$. *Physical Review B* **2024**, *110* (14). DOI: 10.1103/PhysRevB.110.L140407.
- (4) Xu, X.; Wu, L.; Zhu, Y.; Cava, R. J. $\text{K}_2\text{Co}_2\text{TeO}_6$: A layered magnet with a $S = 1/2$ Co^{2+} honeycomb lattice. *Physical Review B* **2023**, *108* (17). DOI: 10.1103/PhysRevB.108.174432.
- (5) Wang, X.; Sharma, R.; Becker, P.; Bohatý, L.; Lorenz, T. Single-crystal study of the honeycomb XXZ magnet $\text{BaCo}_2(\text{PO}_4)_2$ in magnetic fields. *Physical Review Materials* **2023**, *7* (2). DOI: 10.1103/PhysRevMaterials.7.024402.
- (6) van Veenendaal, M.; Poldi, E. H. T.; Veiga, L. S. I.; Bencok, P.; Fabbris, G.; Tartaglia, R.; McChesney, J. L.; Freeland, J. W.; Hemley, R. J.; Zheng, H.; et al. Electronic structure of Co 3d states in the Kitaev material candidate honeycomb cobaltate $\text{Na}_3\text{Co}_2\text{SbO}_6$ probed with x-ray dichroism. *Physical Review B* **2023**, *107* (21). DOI: 10.1103/PhysRevB.107.214443.
- (7) Xie, Y. M.; Wang, C. C. Memory effect of magnetoelectric coupling in antiferromagnetic cobalt tantalate with honeycomb lattice. *Journal of Alloys and Compounds* **2022**, *906*. DOI: 10.1016/j.jallcom.2022.164066.
- (8) Marshall, M.; Wang, F.; Klimczuk, T.; Mudiyansele, R. S. D.; Greenblatt, M.; Walker, D.; Xie, W. $\text{Eu}_2\text{Mg}_3\text{Bi}_4$: Competing Magnetic Orders on a Buckled Honeycomb Lattice. *Chem Mater* **2022**, *34* (9). DOI: 10.1021/acs.chemmater.1c03612.
- (9) Horsley, E.; Rao, X.; Yi, S. B.; Kim, Y. J. Magnetic dilution of a honeycomb lattice XY magnet CoTiO_3 . *J Phys Condens Matter* **2022**, *34* (13). DOI: 10.1088/1361-648X/ac484c From NLM PubMed-not-MEDLINE.
- (10) Lee, N.; Oh, D. G.; Choi, S.; Moon, J. Y.; Kim, J. H.; Shin, H. J.; Son, K.; Nuss, J.; Kiryukhin, V.; Choi, Y. J.; et al. Highly nonlinear magnetoelectric effect in buckled-honeycomb antiferromagnetic $\text{Co}_4\text{Ta}_2\text{O}_9$. *Scientific Reports* **2020**, *10*:1 **2020-07-23**, *10* (1). DOI: 10.1038/s41598-020-69117-5.
- (11) Nair, H. S.; Brown, J. M.; Coldren, E.; Hester, G.; Gelfand, M. P.; Podlesnyak, A.; Huang, Q.; Ross, K. A. Short-range order in the quantum XXZ honeycomb lattice material $\text{BaCo}_2(\text{PO}_4)_2$. *Physical Review B* **2018**, *97* (13). DOI: 10.1103/PhysRevB.97.134409.
- (12) Wong, C.; Avdeev, M.; Ling, C. D. Zig-zag magnetic ordering in honeycomb-layered $\text{Na}_3\text{Co}_2\text{SbO}_6$. *Journal of Solid State Chemistry* **2016**, *243*. DOI: 10.1016/j.jssc.2016.07.032.
- (13) A. Zvereva, E.; I. Stratan, M.; V. Ushakov, A.; B. Nalbandyan, V.; L. Shukaev, I.; V. Silhanek, A.; M. Abdel-Hafiez; V. Streltsov, S.; N. Vasiliev, A.; A. Zvereva, E.; et al. Orbitally induced hierarchy of exchange interactions in the zigzag antiferromagnetic state of honeycomb silver delafossite $\text{Ag}_3\text{Co}_2\text{SbO}_6$. *Dalton Transactions* **2016**, *45* (17). DOI: 10.1039/C6DT00516K.
- (14) Seibel, E. M.; Roudebush, J. H.; Wu, H.; Huang, Q.; Ali, M. N.; Ji, H.; Cava, R. J. Structure and magnetic properties of the alpha- NaFeO_2 -type honeycomb compound $\text{Na}_3\text{Ni}_2\text{BiO}_6$. *Inorg Chem* **2013**, *52* (23), 13605-13611. DOI: 10.1021/ic402131e From NLM PubMed-not-MEDLINE.
- (15) Lee, S.; Choi, S.; Kim, J.; Sim, H.; Won, C.; Lee, S.; Kim, S. A.; Hur, N.; Park, J. G. Antiferromagnetic ordering in Li_2MnO_3 single crystals with a two-dimensional honeycomb

lattice. *J Phys Condens Matter* **2012**, *24* (45), 456004. DOI: 10.1088/0953-8984/24/45/456004
From NLM PubMed-not-MEDLINE.

(16) Singh, Y.; Gegenwart, P. Antiferromagnetic Mott insulating state in single crystals of the honeycomb lattice material Na₂IrO₃. *Physical Review B* **2010**, *82* (6). DOI: 10.1103/PhysRevB.82.064412.

(17) Ham, W. S.; Pradipto, A.-M.; Yakushiji, K.; Kim, K.; Rhim, S. H.; Nakamura, K.; Shiota, Y.; Kim, S.; Ono, T.; Ham, W. S.; et al. Dzyaloshinskii–Moriya interaction in noncentrosymmetric superlattices. *npj Computational Materials* *2021 7:1* **2021**, *7* (1). DOI: 10.1038/s41524-021-00592-8.

(18) Wang, C.; Guo, G.-C.; He, L. Ferroelectricity Driven by the Noncentrosymmetric Magnetic Ordering in Multiferroic TbMnO₄: A First-Principles Study. *Physical Review Letters* **2007**, *99* (17). DOI: 10.1103/PhysRevLett.99.177202.

(19) Cheong, S.-W.; Mostovoy, M.; Cheong, S.-W.; Mostovoy, M. Multiferroics: a magnetic twist for ferroelectricity. *Nature Materials* *2007 6:1* **2007**, *6* (1). DOI: 10.1038/nmat1804.

(20) Spaldin, N. A.; Fiebig, M. The Renaissance of Magnetoelectric Multiferroics. *Science* **2005**. DOI: 10.1126/science.1113357.

(21) Aoyama, T.; Yamauchi, K.; Iyama, A.; Picozzi, S.; Shimizu, K.; Kimura, T.; Aoyama, T.; Yamauchi, K.; Iyama, A.; Picozzi, S.; et al. Giant spin-driven ferroelectric polarization in TbMnO₃ under high pressure. *Nature Communications* *2014 5:1* **2014**, *5* (1). DOI: 10.1038/ncomms5927.

(22) Kimura, T.; Goto, T.; Shintani, H.; Ishizaka, K.; Arima, T.; Tokura, Y.; Kimura, T.; Goto, T.; Shintani, H.; Ishizaka, K.; et al. Magnetic control of ferroelectric polarization. *Nature* *2003 426:6962* **2003**, *426* (6962). DOI: 10.1038/nature02018.

(23) Liu, M.; Zhang, L.; Liu, J.; Wan, T. L.; Du, A.; Gu, Y.; Kou, L. Density Functional Theory Studies on Magnetic Manipulation in NiI₂ Layers. *ACS Applied Electronic Materials* **2023**, *5* (2). DOI: 10.1021/acsaelm.2c01479.

(24) Kurumaji, T.; Seki, S.; Ishiwata, S.; Murakawa, H.; Kaneko, Y.; Tokura, Y. Magnetoelectric responses induced by domain rearrangement and spin structural change in triangular-lattice helimagnets NiI₂ and CoI₂. *Physical Review B* **2013**, *87* (1). DOI: 10.1103/PhysRevB.87.014429.

(25) Zhu, H.; Yu, H.; Zhu, W.; Yu, G.; Xu, C.; Xiang, H. Moir'e-Induced Magnetoelectricity in Twisted Bilayer NiI₂. *Physical Review Letters* **2025**, *135* (19). DOI: 10.1103/p6n8-n1rx.

(26) Jin, C.; Liu, C.; Ren, F.; Wang, B.; Jia, M.; Gu, Q. Magneto-electric coupling beyond van der Waals interaction in two-dimensional multiferroic heterostructures. *Applied Physics Letters* **2023**, *123* (26). DOI: 10.1063/5.0180680.

(27) Zhang, K.-X.; Park, G.; Lee, Y.; Kim, B. H.; Park, J.-G.; Zhang, K.-X.; Park, G.; Lee, Y.; Kim, B. H.; Park, J.-G. Magnetoelectric effect in van der Waals magnets. *npj Quantum Materials* *2025 10:1* **2025**, *10* (1). DOI: 10.1038/s41535-025-00725-y.

(28) Chu, H.; Roh, C. J.; Island, J. O.; Li, C.; Lee, S.; Chen, J.; Park, J.-G.; Young, A. F.; Lee, J. S.; Hsieh, D. Linear Magnetoelectric Phase in Ultrathin MnPS₃ Probed by Optical Second Harmonic Generation. *Physical Review Letters* **2020**, *124* (2). DOI: 10.1103/PhysRevLett.124.027601.

(29) Khanh, N. D.; Abe, N.; Sagayama, H.; Nakao, A.; Hanashima, T.; Kiyanagi, R.; Tokunaga, Y.; Arima, T. Magnetoelectric coupling in the honeycomb antiferromagnet Co₄Nb₂O₉. *Physical Review B* **2016**, *93* (7). DOI: 10.1103/PhysRevB.93.075117.

(30) Ding, L.; Lee, M.; Hong, T.; Dun, Z.; Sinclair, R.; Chi, S.; Agrawal, H. K.; Choi, E. S.; Chakoumakos, B. C.; Zhou, H.; et al. Noncollinear magnetic structure and magnetoelectric

coupling in buckled honeycomb Co₄Nb₂O₉: A single-crystal neutron diffraction study. *Physical Review B* **2020**, *102* (17). DOI: 10.1103/PhysRevB.102.174443.

(31) Zhao, T.; Scholl, A.; Zavaliche, F.; Lee, K.; Barry, M.; Doran, A.; Cruz, M. P.; Chu, Y. H.; Ederer, C.; Spaldin, N. A.; et al. Electrical control of antiferromagnetic domains in multiferroic BiFeO₃ films at room temperature. *Nature Materials* **2006**, *5*:10 **2006**, *5* (10). DOI: 10.1038/nmat1731.

(32) Taniguchi, K.; Abe, N.; Umetsu, H.; Katori, H. A.; Arima, T. Control of the Magnetoelectric Domain-Wall Stability by a Magnetic Field in a Multiferroic MnWO₄. *Physical Review Letters* **2008**, *101* (20). DOI: 10.1103/PhysRevLett.101.207205.

(33) Lebeugle, D.; Colson, D.; Forget, A.; Viret, M.; Bataille, A. M.; Gukasov, A. Electric-Field-Induced Spin Flop in BiFeO₃ Single Crystals at Room Temperature. *Physical Review Letters* **2008**, *100* (22). DOI: 10.1103/PhysRevLett.100.227602.

(34) Hoffmann, T.; Thielen, P.; Becker, P.; Bohatý, L.; Fiebig, M. Time-resolved imaging of magnetoelectric switching in multiferroic MnWO₄. *Physical Review B* **2011**, *84* (18). DOI: 10.1103/PhysRevB.84.184404.

(35) Nelson, R.; Ertural, C.; George, J.; Deringer, V. L.; Hautier, G.; Dronskowski, R. LOBSTER: Local orbital projections, atomic charges, and chemical-bonding analysis from projector-augmented-wave-based density-functional theory. *Journal of Computational Chemistry* **2020**, *41* (21). DOI: 10.1002/jcc.26353.

(36) Maintz, S.; Deringer, V. L.; Tchougréeff, A. L.; Dronskowski, R. LOBSTER: A tool to extract chemical bonding from plane-wave based DFT. *Journal of Computational Chemistry* **2016**, *37* (11). DOI: 10.1002/jcc.24300.

(37) Steinberg, S.; Dronskowski, R.; Steinberg, S.; Dronskowski, R. The Crystal Orbital Hamilton Population (COHP) Method as a Tool to Visualize and Analyze Chemical Bonding in Intermetallic Compounds. *Crystals* **2018**, *Vol. 8*, **2018**, *8* (5). DOI: 10.3390/cryst8050225.

(38) Volker L. Deringer, A. L. T., Richard Dronskowski. Crystal Orbital Hamilton Population (COHP) Analysis As Projected from Plane-Wave Basis Sets. *The Journal of Physical Chemistry A* **2011**, *115* (21). DOI: 10.1021/jp202489s.

(39) Müller, P. C.; Ertural, C.; Hempelmann, J.; Dronskowski, R. Crystal Orbital Bond Index: Covalent Bond Orders in Solids. *The Journal of Physical Chemistry C* **2021**, *125* (14). DOI: 10.1021/acs.jpcc.1c00718.

(40) Liechtenstein, A. I.; Katsnelson, M. I.; Antropov, V. P.; Gubanov, V. A. Local spin density functional approach to the theory of exchange interactions in ferromagnetic metals and alloys. *Journal of Magnetism and Magnetic Materials* **1987**, *67* (1). DOI: 10.1016/0304-8853(87)90721-9.

(41) He, X.; Helbig, N.; Verstraete, M. J.; Bousquet, E. TB2J: A python package for computing magnetic interaction parameters. *Computer Physics Communications* **2021**, *264*. DOI: 10.1016/j.cpc.2021.107938.

(42) Mugiraneza, S.; Hallas, A. M.; Mugiraneza, S.; Hallas, A. M. Tutorial: a beginner's guide to interpreting magnetic susceptibility data with the Curie-Weiss law. *Communications Physics* **2022**, *5*:1 **2022**, *5* (1). DOI: 10.1038/s42005-022-00853-y.

(43) Li, Y.; Winter, S. M.; Kaib, D. A. S.; Riedl, K.; Valentí, R. Modified Curie-Weiss law for J_{eff} magnets. *Physical Review B* **2021**, *103* (22). DOI: 10.1103/PhysRevB.103.L220408.

(44) Huai, X.; Cairns, L. P.; Delles, B.; Winiarski, M. J.; Sorolla II, M.; Zhang, X.; Chen, Y.; Calder, S.; Kanyowa, T.; Kogar, A.; et al. Jeff = 1/2 Diamond Magnet CaCo₂TeO₆: A Pathway toward New Spin Physics and Quantum Functions. **2025**. DOI: 10.48550/arXiv.2503.18977.

